Scattering of Ice Particles at Microwave Frequencies: A Physically Based Parameterization

MIN-JEONG KIM

Department of Atmospheric and Oceanic Sciences, University of Wisconsin—Madison, Madison, Wisconsin, and Goddard Earth Sciences and Technology Center, University of Maryland, Baltimore County, Baltimore, Maryland

MARK S. KULIE, CHRIS O'DELL, AND RALF BENNARTZ

Department of Atmospheric and Oceanic Sciences, University of Wisconsin—Madison, Madison, Wisconsin

(Manuscript received 9 January 2006, in final form 6 July 2006)

ABSTRACT

This paper presents a new, purely physical approach to simulate ice-particle scattering at microwave frequencies. Temperature-dependent ice particle size distributions measured by aircraft in midlatitude frontal systems are used to represent the distribution of precipitation-sized frozen hydrometeors above the freezing level through derived radar reflectivity–snow water content (Z–M) relationships. The discrete dipole approximation is employed to calculate optical properties of selected types of idealized nonspherical ice particles (hexagonal columns, four-arm rosettes, and six-arm rosettes). Based on those assumptions, passive microwave optical properties are calculated using radar observations from Gotland Island in the Baltic Sea. These forward-simulated brightness temperatures are compared with observed data from both the Advanced Microwave Scanning Radiometer (AMSR-E) and the Advanced Microwave Sounding Unit-B (AMSU-B). Results show that the new ice scattering/microphysics model is able to generate brightness temperatures that are consistent with AMSR and AMSU-B observations of two light-winter-precipitation cases. The overall differences among the various ice-habit results at 89 GHz are generally not that expansive, whereas the AMSU-B 150-GHz comparisons show increased sensitivity to ice-particle shapes.

1. Introduction

With the success of the Tropical Rainfall Measuring Mission (TRMM), satellite-based remote sensing has become a key tool for understanding tropical precipitation. The TRMM's successor, the Global Precipitation Measurement (GPM) is on the horizon and will extend the unique capabilities of combined radar and passive microwave observations to higher latitudes.

Extratropical precipitation is, in general, shallower than tropical precipitation and generally exhibits a lower freezing level. Thus, low-frequency channels that are sensitive to the column amount of liquid rain are only of limited use to derive precipitation estimates at mid- and high latitudes. Passive microwave precipitation estimates therefore have to rely more strongly on high-frequency observations (>50 GHz) that are more sensitive to precipitation-sized ice particles.

In contrast to low-frequency passive microwave observations, radiative transfer at higher frequencies depends strongly on the scattering properties of the ice particles above the melting layer. In particular, two aspects have to be dealt with when approaching high-frequency passive microwave radiative transfer in precipitating clouds. The first issue is related to the size distribution of the falling ice particles above the freezing level. The second aspect is related to the shape of individual ice particles and their resulting scattering properties. Both the size distribution and the particle scattering properties are not well known, and several simplifying assumptions have been made in the literature.

A commonly used simplifying assumption is that ice particles can be represented by soft spheres composed of a mixture of ice and air, which for a given dielectric mixing rule reduces the number of degrees of freedom

Corresponding author address: Min-Jeong Kim, NASA Goddard Space Flight Center, Mail Code 614.6, Greenbelt, MD 20771.
E-mail: min-jeong.kim@noaa.gov

DOI: 10.1175/JAM2483.1

that determine the radiative transfer problem to one, which is the density of the particle. This approach is, for example, used in Bennartz and Petty (2001, hereinafter BP2001) and Bauer et al. (1999) as well as in many other studies. Several authors (Liu 2004; Johnson and Petty 2004; Kim 2006) have pointed out, however, that scattering parameters obtained for spherical particles do not agree well with those obtained for more realistic nonspherical particles. In addition, the particular and, to some extent, arbitrary choice of the dielectric mixing rule imposes large variations on the scattering parameters obtained.

Both the choice of the particle size distribution (PSD) and the ice-particle scattering model strongly affect the simulated brightness temperatures at frequencies higher than about 50 GHz. Several authors try to resolve one or both issues by empirically tuning the size distribution to fit observed brightness temperature depressions in precipitating areas. BP2001 introduce an empirical tuning factor that relates the average diameter of an exponential size distribution of ice particles (using the liquid equivalent radius) to a Marshall–Palmer reference size distribution (Marshall and Palmer 1948) for liquid precipitation. Although this parameter can be used to tune the ice scattering for a wide variety of different cases, its purely empirical definition is unsatisfactory, and it is unclear whether the results obtained using this (or similar methods) can be extrapolated to different frequencies. Other authors use the PSDs that were derived for falling snow (e.g., Sekhon and Srivastava 1970) or use similar ad hoc parameters to modify the size distribution. Results are, in general, not satisfactory and are in poor agreement with observations.

Some authors attempted to circumvent the problems inherent in the treatment of ice-particle scattering and size distribution by using empirical retrieval algorithms. For example, Bennartz et al. (2002) used radar-derived probability density distribution functions of precipitation amount to derive precipitation likelihoods from Advanced Microwave Sounding Unit (AMSU)-A/-B data. In a somewhat similar approach, Chen and Staelin (2003) used a neural network trained on AMSU-A/-B data versus Next-Generation Weather Radar (NEXRAD) precipitation estimates. Kongoli et al. (2003) developed an empirical method to detect snowfall over land using the AMSU-B-observed brightness temperatures. Although such approaches are beneficial and produce algorithms that allow one to estimate precipitation likelihood or intensity, for example, in an operational nowcasting environment, their usefulness in understanding possibly subtle climate-related signals is limited, and, once established, the relation between scattering intensity at a given frequency and rain rate remains fixed until a new training is obtained or the underlying rainfall probability density distribution functions are changed. To fully use passive microwave data for high-latitude precipitation estimation, physical models are needed to understand how ice crystals and their corresponding size distribution affect the radiative transfer process at microwave frequencies.

Within this paper we present a new, purely physical approach to simulate ice-particle scattering at microwave frequencies. The approach we take incorporates both realistic size distributions for the ice particles above the melting layer and scattering parameters that account for their nonspherical particle shape. In a manner similar to BP2001, we calculate passive microwave optical properties from observed radar reflectivity data and compare forward-simulated brightness temperatures with observed data both from the Advanced Microwave Scanning Radiometer (AMSR-E, hereinafter referred to as AMSR for brevity) and the AMSU-B. These comparisons allow us to evaluate the representativeness of the PSD and the scattering parameters in observation space in terms of deviations between observed and simulated brightness temperatures over a wide spectral range.

Section 2 describes the active and passive microwave measurements employed in this study and the method used to combine the data. Section 3 presents the single-scattering parameterization method to represent the observed ice PSDs, radar reflectivities, and microwave brightness temperatures. Two light-winter-precipitation cases employed in this study are described in section 4. Simulation results and comparisons with AMSR-E and AMSU-B observations are presented in section 5. Sections 6 and 7 present a discussion and conclusions, respectively.

2. Data and methods

This study uses data from various active and passive microwave remote sensing instruments. Section 2 provides a brief overview of the data employed.

a. Radar data

The radar data used in this study were collected by a C-band Doppler radar located near Hemse, Sweden, which is located on Gotland Island in the Baltic Sea. This radar is jointly operated by the Swedish Meteorological and Hydrological Institute and Swedish Air Force and is also a component of the Baltic Sea Experiment (BALTEX) Radar Network (BALTRAD). This particular radar is ideal for our scientific purposes because its high-latitude location frequently samples

frozen winter precipitation and warm-season precipitation events that have relatively low freezing levels. In addition, the Hemse radar data are useful for evaluating passive microwave data because much of its domain is located over the Baltic Sea, which provides a fairly uniform cold background in the microwave spectrum that makes it easier to detect passive microwave signatures of precipitation when compared with the high microwave emissivities of land surfaces. The radar data were obtained from the BALTEX Data Radar Centre (BRDC), which archives and distributes BALTRAD data and products in a standard format (Michelson et al. 2000, 2002).

Radar data were collected at the following 12 elevation angles for each polar volume scan: 0.5°, 0.7°, 0.9°, 1.1°, 1.5°, 2.3°, 3.2°, 4.1°, 6.0°, 12.0°, 24.0°, and 40.0°. As a first processing step, each volume scan was mapped to a quality-controlled composite reflectivity map generated by the BRDC, and any spurious radar echoes not associated with precipitation were removed. The BRDC quality-control algorithm uses a combination of Meteosat geostationary satellite brightness temperatures and measured 2-m temperatures to flag radar reflectivities that are not likely to be produced by precipitation (Michelson et al. 2000). Next, the polar volumes were transformed into a 240 km × 240 km × 10 km three-dimensional Cartesian grid with a vertical (horizontal) spacing of 1 km (2 km) using a pseudo-CAPPI approach (BP2001). Liquid and frozen hydrometeor size distributions and layer optical properties were created using these gridded radar datasets and were subsequently used as input for a radiative transfer model (see section 2d and section 3).

b. AMSR

The AMSR is a five-frequency (6.925, 10.65, 18.7, 23.8, 36.5, and 89.0 GHz), conically scanning microwave radiometer that is one of six instruments flying on the National Aeronautics and Space Administration (NASA) *Aqua* satellite. The *Aqua* satellite follows a sun-synchronous, near-polar orbit at about 700-km altitude, thus allowing the AMSR instrument to sense upwelling radiation along a total swath width of 1445 km.

Both vertically and horizontally polarized measurements are available for all channels. The AMSR local zenith angle is nearly fixed at about 55° while the local azimuth angle varies and depends on the position of a point on the earth's surface relative to the center line of each AMSR scan. This study utilizes the AMSR 89-GHz frequency because of its demonstrated sensitivity to frozen, precipitation-sized hydrometeors (Liu and Curry 1997; Katsumata et al. 2000). The effective footprint size of the AMSR 89-GHz channel is roughly 6 × 9 km^2.

c. AMSU-B

The AMSU-B is a cross-track-scanning radiometer flown on the *National Oceanic and Atmospheric Administration* (*NOAA*)*-15*, *-16*, and *-17* satellites (Saunders et al. 1995). The instrument has five channels (89.0, 150.0, and 183.3 ± 1, ±3, and ±7 GHz), and its main task is to retrieve atmospheric water vapor profiles. The footprint size is 20 × 16 km^2 for the nadir but increases to 64 × 52 km^2 for the outermost scan angle (~60°).

d. Combining data

We employ a similar scheme as discussed in BP2001 to prepare input fields for radiative transfer modeling that are derived from ground-based radar data. The ultimate goal of this process is to generate simulated brightness temperatures that can be used to assess our microphysical parameterizations using microwave remote sensing techniques. We are also using this exercise as an AMSR and AMSU-B validation effort to evaluate these instruments against another data source.

The first step in this process is to obtain water vapor and cloud liquid water content fields from the standard AMSR level-2 ocean product (Wentz 1997). After applying quality control criteria that ensure the selection of only overwater pixels located outside of heavy precipitation that are not contaminated by sea ice, a kriging technique is used to interpolate the native AMSR data fields to get liquid water content (LWC) and water vapor content (WVC) fields that are matched to the radar grid. As in BP2001, the LWC field is evenly distributed between an assumed cloud base of 1 km and the freezing level and the water vapor is distributed vertically depending on the relative humidity. The freezing level is derived from the AMSR water vapor field (Petty 1994a,b), which allows a temperature field with the same dimensions as the water vapor path (WVP) grid to be built by applying a constant lapse rate of 6.5 K km^{-1} above and below the freezing level. Appropriate radar reflectivity Z and ice water content M or rain-rate R relationships are then applied to convert the reflectivity fields into precipitation rates or snow water content depending on what microphysical parameterization is used (see section 3). In addition, the radar-beam model discussed in BP2001 is employed to adjust the Z–R relationships at longer distances from the radar and to account for melting-level and beam-filling effects. One notable difference, however, between our current work and BP2001 is that we utilize coincident Moderate-Resolution Imaging Spectroradi-

ometer (MODIS) brightness temperature data to create a grid of approximate echo-top heights that are used to weight properly the amount of frozen precipitation in each grid box. (BP2001 used an estimated static cloud-top height for the entire radar domain based on 3D reflectivity profiles). MODIS channel-31 brightness temperatures that are located nearest to each respective radar grid point are converted to physical temperatures. These physical temperatures, which are considered to be a decent proxy of the cloud-top temperature, are then compared with the AMSR-derived vertical temperature profile to approximate the cloud-top height that coincides with each radar pixel. Optical properties are then calculated using either Mie theory or the discrete dipole approximation (DDA)-based method described in section 3.

Proper azimuth- and zenith-viewing angles also need to be considered before performing radiative transfer modeling. For the AMSR data, a constant zenith angle of 55° is used and a 240 km × 240 km azimuth grid that is coincident with the radar data is built using the same kriging technique that is applied to the WVP and LWC fields. Because the AMSU-B is a cross-track-scanning instrument, azimuth and zenith grids have to be constructed from the native data. Surface temperatures and wind speeds from the National Centers for Environmental Prediction's (NCEP) Global Data Assimilation System (GDAS) are used as input to calculate ocean surface emissivities using the Fast Emissivity Model (FASTEM2) (English and Hewison 1998; Deblonde and English 2000). The optical and surface properties are then used as input into a backward Monte Carlo model (Petty 1994b) to simulate brightness temperatures at the various frequencies of interest. The simulated brightness temperatures are convolved to AMSR and AMSU-B footprints using the techniques outlined in Bennartz (2000). Note that the AMSU-B effective field of view varies in size and orientation because of its scanning strategy, and so the function described in Bennartz (2000) is used to determine properly the cross- and along-track footprint size and orientation before the convolution is performed. The convolved simulated brightness temperatures are then compared with AMSR and AMSU-B brightness temperatures using only overwater pixels based on a land/sea mask of the Baltic Sea region.

3. Microphysics parameterizations

a. BP2001 method

BP2001 investigated the effect of variable size distribution and density of precipitation ice particle on microwave brightness temperatures at SSM/I frequencies. A set of self-consistent relationships among rain rate, size parameters of an exponential drop size distribution, and the radar reflectivity–rain-rate relations for frozen and liquid precipitation were derived. The study introduced a scaling factor x, which is the ratio between the average melted diameter of frozen and liquid precipitation and is given by

$$\frac{\int_0^\infty N_L(D)D\,dD}{\int_0^\infty N_L(D)\,dD} = x\,\frac{\int_0^\infty N_F(D)D\,dD}{\int_0^\infty N_F(D)\,dD}, \qquad (1)$$

where $N(D)$ is an exponential PSD and the subscripts L and F refer to liquid and frozen precipitation, respectively.

The approach allowed the different sizes of the frozen particles to vary, but the size distributions were constrained to depend on the raindrop size distributions, which were assumed to follow Marshall and Palmer (1948). The best-match PSDs of frozen particles determined by this size ratio guarantee a consistent relation between the 89-GHz passive microwave scattering index, ice water content, and radar reflectivity. The scattering index, as introduced by Petty (1994a,b), is a linear combination of the vertically and horizontally polarized brightness temperature T_b and is defined as

$$S_{89} = P_{89}\mathrm{T_B89v_0} + (1 - P_{89})T_c - \mathrm{T_B89v}, \qquad (2)$$

where the attenuation index P_{89} is

$$P_{89} = \frac{\mathrm{T_B89v} - \mathrm{T_B89h}}{\mathrm{T_B89v_0} - \mathrm{T_B89h_0}}, \qquad (3)$$

T_c is the unpolarized limiting brightness temperature of an optically thick liquid water layer, $\mathrm{T_B89v}$ ($\mathrm{T_B89h}$ is the observed 89-GHz vertically (horizontally) polarized brightness temperature, and $\mathrm{T_B89v_0}$ ($\mathrm{T_B89h_0}$) is the hypothetical vertically (horizontally) polarized 89-GHz brightness temperature in a cloud-free region. The scattering index estimates the T_b depression relative to emission from a nonscattering atmosphere whose total transmittance yields the same degree of polarization and allows one to isolate effectively the effects of scattering. The BP2001 approach thus overcomes the limitations of assuming a fixed ice PSD such as the one by Sekhon and Srivastava (1970). However, as shown in the subsequent investigations, it is not guaranteed that a given size ratio yields consistent results for the observations at multiple passive microwave frequencies.

The next section introduces an improved microphysics parameterization of frozen particles following BP2001. This new physically based microphysics parameterization of ice crystals seeks to generate consis-

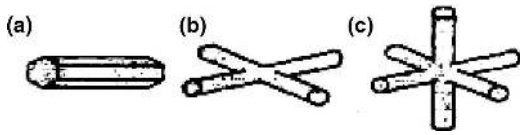

FIG. 1. Ice crystal models considered in this study: (a) HC, (b) R4, and (c) R6.

tent ice water content, radar reflectivity, and scattering indices simultaneously over the entire passive microwave spectral range.

b. Ice crystal models and single scattering calculations

Figure 1 shows ice crystal models considered in this study: hexagonal columns (HC), planar rosettes with four arms (R4), and spatial rosettes with six arms (R6). Following Hobbs et al. (1974), the relationship between diameter D and length L for hexagonal columns considered in this study is given by

$$\ln D_{\mathrm{mm}} = -0.6524 + 1.32 \ln L_{\mathrm{mm}} - 0.0846(\ln L_{\mathrm{mm}})^2. \tag{4}$$

The R4s and R6s are modeled with two and three circular cylinders having the same aspect ratio as a single hexagonal column.

The ice density is assumed to be the same as pure ice in this study. The real (ε') and imaginary (ε'') parts of dielectric constants measured by Mätzler and Wegmüller (1987) are employed. They found frequency-independent ε' values near 3.17 and a slight dependence on temperature given by

$$\varepsilon' = 3.1884 + 0.000\,91T, \tag{5}$$

and their ε'' is given by

$$\varepsilon'' = A/f + Bf^C, \tag{6}$$

where f is frequency (GHz) and T is temperature (°C). They determined that the empirical constants $A = 3.5 \times 10^{-4}$, $B = 3.6 \times 10^{-5}$, and $C = 1.2$ at $T = -15$°C and $A = 6 \times 10^{-4}$, $B = 6.5 \times 10^{-5}$, and $C = 1.07$ at $T = -5$°C. This study employs Eqs. (5) and (6) for dielectric constants of ice at $T = -15$°C. Test results (not shown in this paper) suggested that changing the dielectric constant with temperature did not make significant differences (less than 1%) in scattering properties at frequencies considered in this study.

This study employs the DDA method to calculate the optical properties of nonspherical ice particles instead of using a mixing formula to calculate scattering parameters. The DDA is a flexible technique for calculating the electromagnetic scattering and absorption by particles with arbitrary shapes and composition (Draine 1988; Mishchenko et al. 2000). The DDA consists of approximating the actual particle by an array of dipoles. Each of the dipoles is subject to an electric field that is the sum of the incident wave and the electric fields resulting from all of the other dipoles. Through the solution of the electric field at each dipole position, the scattering and absorption properties of the particle can be obtained. The DDA replaces the solid particle with an array of point dipoles occupying positions on a cubic lattice, and the lattice spacing must be small relative to the wavelength of the incident light in the particle. Therefore, the DDA method requires large computer storage and central processing unit time. The technique is not suited well for particles with very large complex refractive index n because it requires a much narrower distance between dipoles, thereby requiring much larger memory size. This study employs the DDA codes developed by Draine and Flatau (2003). Details of the DDA theory are described in Draine (1988), Draine and Flatau (1994), and Mishchenko et al. (2000).

c. PSDs

The knowledge of the shape of PSD is crucial for calculations of precipitation rate, radar reflectivity, and radiative extinction properties within a large volume of atmosphere. One of the largest uncertainties in optical calculations of precipitating particles is caused by the unknown PSDs (BP2001). Various hydrometeor size distributions and radar reflectivity–frozen-precipitation-rate relations have been reported (Sekhon and Srivastava 1970; Hobbs et al. 1974; Fujiyoshi et al. 1990). Based on radar reflectivity measurements, precipitation rate, and/or ice-particle sizes, these studies suggested exponential PSDs. However, their measurements were made near the ground, and so the dependence of particle sizes on environmental air temperature was not fully considered in their parameterizations, although the size distributions of snow crystals are known to vary with altitude and air temperature.

Heymsfield and Platt (1984) and Heymsfield et al. (2002) sought to parameterize ice PSDs by aircraft observations in cirrus and suggested that the crystal spectra changed systematically with temperature. Field et al. (2005) recently analyzed PSDs measured by the U.K. C-130 aircraft in ice clouds (nimbostratus, altostratus, cumulostratus, and cirrus) associated with midlatitude frontal systems around the British Isles. Finding power laws relating moments of the size distributions, they developed a model predicting ice PSDs for a given air temperature.

The generalized scaling function that can be used to

represent the size distributions of ice crystals is given by Lee et al. (2004) for any pair of moments of the PSD,

$$N(D) = M_i^{(j+1)/(j-i)} M_j^{(i+1)/(i-j)} \phi_{ij}(x), \quad \text{where} \tag{7}$$

$$x = D(M_i/M_j)^{1/(j-i)}, \tag{8}$$

ϕ_{ij} is the universal function that is scaled to give the observed PSD, and M_n is PSD moments of order n. It is defined by

$$M_n = \int_0^\infty D^n N(D)\, dD \approx \sum_{D_{\min}}^{D_{\max}} D^n N_D, \tag{9}$$

where D in meters is a particle size parallel to the flight direction, $N(D)dD$ is the concentration of particles with sizes between D and $D + dD$, and N_D is the particle concentration in the size bin with size D.

The combination of moments prefixing the universal distribution has previously been termed N_0^* $[\equiv M_i^{(j+1)/(j-i)} M_j^{(i+1)/(i-j)}]$ by Illingworth and Blackman (1999) for rain and by Tinel et al. (2005) for ice particles. Field et al. (2005) found that the second ($i = 2$) and third ($j = 3$) measured moments have an exponential relationship with in-cloud temperature T_c (°C) given by

$$N_{0,23}^* = (5.65 \times 10^5) \exp(-0.107 T_c) \tag{10}$$

(m^{-4}). The study also suggested power laws for different moments of order n for each temperature interval given by

$$M_n = a(n, T_c) M_2^{b(n,T_c)}. \tag{11}$$

Following Field et al. (2005), exponents $b(n, T_c)$ and coefficients $a(n, T_c)$ of these power laws are given by

$$\log_{10} a(n, T_C) = a_1 + a_2 T_C + a_3 n + a_4 T_c n + a_5 T_C^2 + a_6 n^2 + a_7 T_C^2 n + a_8 T_C n^2 + a_9 T_C^3 + a_{10} n^3 \quad \text{and} \tag{12}$$

$$b(n, T_C) = b_1 + b_2 T_C + b_3 n + b_4 T_c n + b_5 T_C^2 + b_6 n^2 + b_7 T_C^2 n + b_8 T_C n^2 + b_9 T_C^3 + b_{10} n^3, \tag{13}$$

where constants $a_1, \ldots, a_{10}$ and $b_1, \ldots, b_{10}$ are shown in Table 1. Using $N_{0,23}^*$ of Field et al. (2005), we employ second and third moments of PSDs in Eqs. (7)–(9).

Note that size distributions of ice particles shown in Field et al. (2005) and in Westbrook et al. (2004a,b) are bimodal and differ from a simple exponential function. For large particles, the size distribution appears exponential as expected, but, for small particles, the size distribution is much steeper. Taking into account the existence of the narrow peak in small particle size ranges, Field et al. (2005) presented fits to each rescaled distribution using a combination of exponential and gamma distributions. Following Field et al. (2005, their Table 3),

TABLE 1. Constants used in Eqs. (10)–(11) for coefficients and exponents of moment power laws (from Field et al. 2005).

x	a_x	b_x
1	5.065 339	0.476 221
2	−0.062 659	−0.015 896
3	−3.032 362	0.165 977
4	0.029 469	0.007 468
5	−0.000 285	−0.000 141
6	0.312 550	0.060 366
7	0.000 204	0.000 079
8	0.003 199	0.000 594
9	0.000 000	0.000 000
10	−0.015 952	−0.003 577

$$\phi_{2,3}(x) = 490.6 \exp(-20.78x) + 17.46x^{0.6357} \times \exp(-3.290x). \tag{14}$$

After putting Eqs. (8), (10), (11), and (14) into Eq. (7), the final form of PSDs used in this study is given by

$$N(D_{\text{mm}}) = A_1 \exp(-A_2 \Lambda D_{\text{mm}}) + A_3 \Lambda^{0.6357} D_{\text{mm}}^{0.6357} \times \exp(-A_4 \Lambda D_{\text{mm}}) \tag{15}$$

($\text{mm}^{-1}\ \text{m}^{-3}$), where D_{mm} is the large dimension of the ice particle (mm),

$$A_1 = 0.4906 N_{0,23}^*(T_c),$$

$$A_2 = 0.020\,78[a(3, T_c)]^{-1},$$

$$A_3 = N_{0,23}^*(T_c) 0.017\,46 \times 10^{-1.9071} [a(3, T_c)]^{-0.6357},$$

$$A_4 = 0.003\,29[a(3, T_c)]^{-1}, \quad \text{and}$$

$$\Lambda \equiv M_2^{1-b(3,T_c)}.$$

Here $N_{0,23}^*(T_c)$ has units of meters to the negative fourth power.

d. Derivations of radar reflectivity Z and snow water content M

Power-law relationships between DDA-calculated backscattering cross sections (σ_b) in 14 discrete particle sizes at 5.65-GHz frequency (of the Gotland Island radar) and large dimension of particle size have been derived by fitting curves and are given by

$$\sigma_b = p D_{\text{mm}}^q \tag{16}$$

(mm^2), where values of the two constants p and q for different particles are given in the Table 2. The effec-

TABLE 2. Relationships between DDA-calculated backscattering cross sections σ_b and large dimension of particle size ($\sigma_b = pD_{\rm mm}^q$).

	P	q	$V(D_{\rm mm})$
Hexagonal columns	$10^{-6.9521}$	5.7273	$0.036\,73D_{\rm mm}^{2.876}$
Planar rosettes with four arms	$10^{-6.2447}$	5.7380	$0.088\,83D_{\rm mm}^{2.876} - 0.008\,965D_{\rm mm}^{2.814}$
Spatial rosettes with six arms	$10^{-5.9339}$	5.7475	$0.1332D_{\rm mm}^{2.876} - 0.017\,93D_{\rm mm}^{2.814}$

tive radar reflectivity factor Z is defined as the average of the backscattering cross sections over a PSD:

$$Z = \frac{\lambda^4}{(\pi^5|K|^2)} \int \sigma_b N(D_{\rm mm})\, dD_{\rm mm} \tag{17}$$

($\rm mm^6\ m^{-3}$), where λ (mm) is the wavelength of the radar, $K = (m^2 - 1)/(m^2 + 2)$, and m is the complex refractive index for water at a given frequency. After putting Eqs. (15) and (16) into Eq. (17),

$$\begin{aligned} Z &= C^* p A_1 \int_0^\infty D_{\rm mm}^q \exp(-A_2 \Lambda D_{\rm mm})\, dD_{\rm mm} + C^* p A_3 \Lambda^{0.6357} \int_0^\infty D_{\rm mm}^{q+0.6357} \exp(-A_4 \Lambda D_{\rm mm})\, dD_{\rm mm} \\ &= C^* p A_1 \frac{\Gamma(q+1)}{(A_2\Lambda)^{q+1}} + C^* p A_3 \Lambda^{0.6357} \frac{\Gamma(q+1.6357)}{(A_4\Lambda)^{q+1.6357}}, \end{aligned} \tag{18}$$

where $C^* = \lambda^4/(\pi^5|K|^2)$ and the Γ symbol represents the gamma function. For a given ice PSD, precipitation water content M ($\rm g\ m^{-3}$) is approximated with 14 finite particle sizes considered in the DDA calculations of Kim (2006):

$$M = \int_{D_{\rm min}}^{D_{\rm max}} \rho_i V(D) N(D)\, dD \approx \rho_i \sum_{i=1}^{i=14} V(D_i) N(D_i) \Delta D_i, \tag{19}$$

where ρ_i ($=0.91$ g $\rm cm^{-3}$) is the density of ice and $V(D_{\rm mm})$ is the volume of an ice crystal for a given particle size.

e. Retrievals of snow water content M and ice PSDs from the observed radar reflectivity

Details of the radar-beam model for the Gotland radar reflectivities are described in BP2001. The model derives the relative weights associated with liquid and frozen precipitation by integrating the antenna pattern function over the altitude range that is covered by the precipitation type.

There is only one free parameter (M_2) in the size distributions of frozen precipitation for a given atmospheric temperature T_c in Eq. (15). If there is any observed parameter, this unknown free parameter can be determined. Because radar reflectivities are given as observations, a PSD can be determined.

Because it is not possible to solve M_2 in terms of M analytically because of the summed form of gamma and exponential functions, empirical relationships between M_2 and M have been found and are given by

$$\log_{10}(M_2) = \xi_0 + \xi_1(\log_{10}M) + \xi_2(\log_{10}M)^2 + \xi_3(\log_{10}M)^3, \tag{20}$$

and values for constants ξ_0, ξ_1, ξ_2, andξ_3 are given in Table 3 for different particle shapes for a given temperature.

In this study, snow water content M values ranging between 0.001 and 2 g $\rm m^{-3}$ are iteratively employed, and the corresponding M_2 values and radar reflectivity for a given atmospheric temperature are computed on each iteration using Eq. (20) and Eq. (18), respectively. By finding the calculated radar reflectivity that is most consistent with the observed radar reflectivity, the best-fit M_2 value is determined and the corresponding snow water content value is retrieved.

The old parameterization method used in BP2001 to determine the snow water content is replaced by this new microphysics parameterization method to determine the frozen precipitation water content in the beam model of BP2001.

f. Optical properties for brightness temperature calculations

Using the observed radar reflectivities, size distributions of ice particles and frozen precipitation water content have been determined for a given temperature and for different particle shapes. In a similar way, optical properties such as extinction coefficients $k_{\rm ext}$, scattering coefficients $k_{\rm sca}$, single scattering albedo $\overline{\omega}$, and asymmetry factors $\overline{g}$ averaged over a PSD are calculated using the DDA-calculated single-scattering properties.

TABLE 3. Relationships between the second moment of size distribution M_2 and frozen precipitation water content M $[\log_{10}M_2 = \xi_0 + \xi_1(\log_{10}M) + \xi_2(\log_{10}M)^2 + \xi_3(\log_{10}M)^3]$.

	T_c (°C)	0	−6.5	−13	−19.5	−26	−32.5	−39.2	−45.5	−52	−58.5
HC	ξ_0	−1.621	−1.440	−1.196	−0.789	−0.156	0.997	2.459	4.305	6.556	8.525
	ξ_1	1.289	1.380	1.304	1.235	1.384	1.863	2.360	2.978	3.723	4.381
	ξ_2	0.254	0.283	0.186	0.033	0.000	0.000	0.000	0.000	0.000	0.000
	ξ_3	0.028	0.036	0.024	0.000	0.000	0.000	0.000	0.000	0.000	0.000
R4	ξ_0	−2.029	−1.884	−1.627	−1.208	−0.626	0.307	1.679	3.529	5.944	7.895
	ξ_1	1.161	1.147	1.139	1.260	1.384	1.785	2.358	3.115	4.095	4.851
	ξ_2	0.250	0.210	0.129	0.087	0.000	0.000	0.000	0.000	0.000	0.000
	ξ_3	0.032	0.029	0.018	0.013	0.000	0.000	0.000	0.000	0.000	0.000
R6	ξ_0	−2.209	−2.062	−1.806	−1.407	−0.847	0.022	1.303	3.033	5.292	7.123
	ξ_1	1.083	1.082	1.099	1.232	1.383	1.783	2.356	3.113	4.092	4.847
	ξ_2	0.235	0.196	0.120	0.080	0.000	0.000	0.000	0.000	0.000	0.000
	ξ_3	0.032	0.029	0.018	0.0125	0.000	0.000	0.000	0.000	0.000	0.000

These optical properties are shown in Fig. 2, for the example of 150 GHz. Figure 2a shows the extinction cross section per unit mass k_{ext}/M. Temperature clearly has a large impact; the two temperatures shown, −5° and −40°C, lead to roughly an order of magnitude of difference in the extinction. Because of the lack of temperature dependence in the index of refraction, this effect is due entirely to the size distribution. The differences among the different habits are smaller but nonnegligible. The mass absorption coefficient (Fig. 2b) is not a very strong function of M or temperature and is much smaller than the total extinction for most tem-

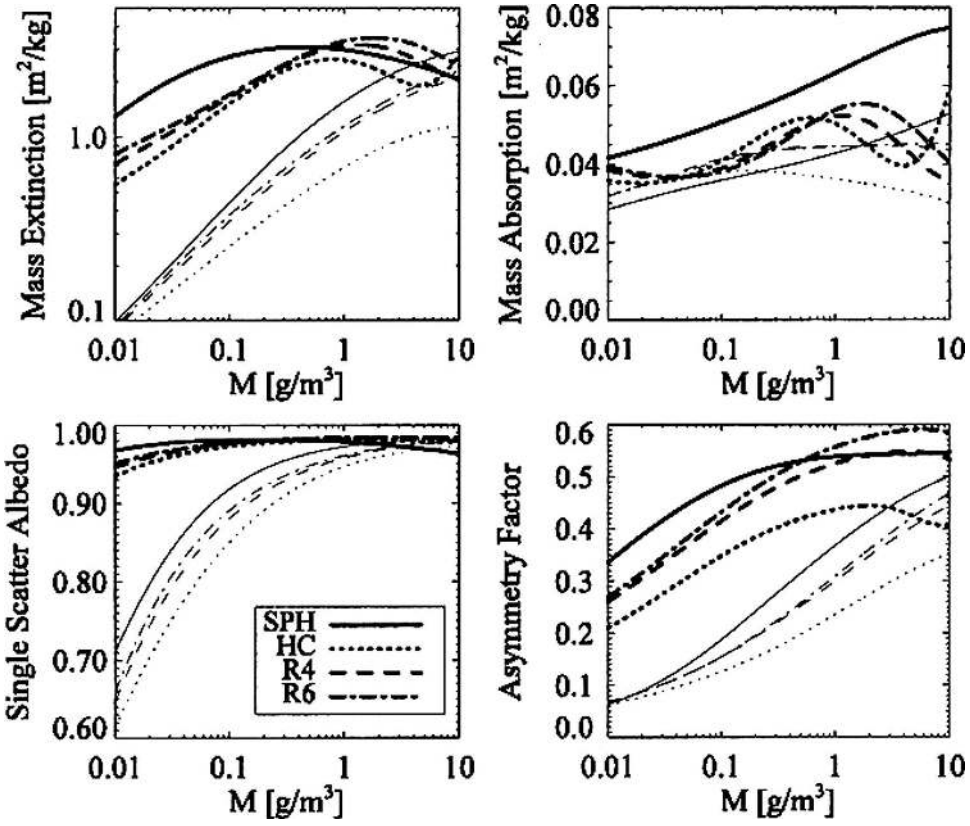

FIG. 2. Selected 150-GHz optical properties of the ice crystal habits employed in this study, calculated as a function of snow water content M. In addition to the habits discussed in the text, spheres (SPH) are shown for comparison. Thick curves are for −5°C crystals; thin curves are for −40°C crystals.

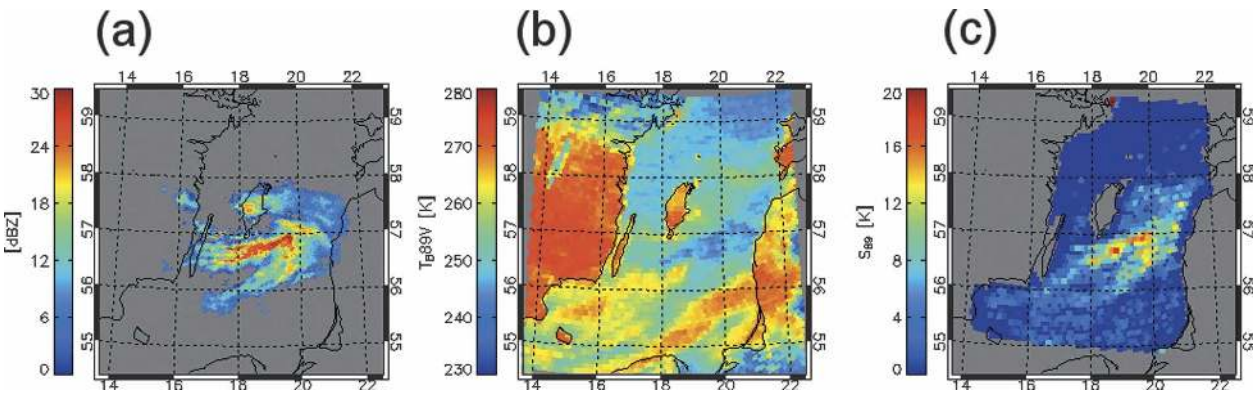

FIG. 3. (a) Hemse radar reflectivity, (b) AMSR-E T_B89V, and (c) AMSR-E S_{89} near 0130 UTC 12 Jan 2003.

peratures, except for the very smallest values of *M*. This is reflected in the high values of single-scatter albedo, especially at −5°C, as shown in Fig. 2c. In addition, Figure 2d shows there is substantial variation in the asymmetry parameter as a function of *M*, temperature, and habit.

4. Case studies

Two case studies have been chosen to demonstrate the new microphysical parameterization described in the previous section. Sections 4a and 4b provide an overview of the case studies.

a. Case 1—12 January 2003

The first selected case occurred near 0130 UTC 12 January 2003. As Fig. 3a shows, a large comma-shaped shield of light to moderate precipitation was mainly located in the southeast quadrant of the Hemse radar scope at 0130 UTC. This precipitation event was located in the warm sector of a strong occluded frontal system that stretched across the Baltic Sea region at 0000 UTC. The maximum radar reflectivity exceeded 30 dB*Z*, and the average echo-top height was about 4–5 km. Surface precipitation rates derived from gauge-adjusted BALTRAD data were near 3 mm h^{-1} in small pockets of the heaviest precipitation, but the majority of surface rain rates were less than 2 mm h^{-1}. The domain-average AMSR-derived freezing level was about 500 m, although the freezing level heights varied between about 200 and 1000 m from the northern to the southern part of the radar domain. Integrated WVPs retrieved by AMSR exceeded 14 kg m^{-2} to the south and southwest of Gotland Island, whereas lower amounts near 9 kg m^{-2} were derived outside of the precipitation to the north of Gotland Island. Maximum values of AMSR-derived columnar liquid water paths (LWP) exceeding 0.3 kg m^{-2} were located in the extreme southeast part of the radar domain, whereas LWP values elsewhere ranged from about 0.05 to 0.15 kg m^{-2}. Winds derived from AMSR data exceeded 10 m s^{-1} throughout the region, and the 2-m temperature near Gotland Island obtained from the NCEP GDAS analysis was 2.5°C. The vertical temperature profile (also constructed from NCEP GDAS data) revealed subfreezing temperatures well below the 850 hPa level near Gotland Island. This information, combined with the AMSR-derived freezing levels, indicates a high likelihood of frozen precipitation reaching the surface throughout this region. The *Aqua* satellite orbited the region near 0131 UTC, and the AMSU-B instrument on the *NOAA-16* satellite flew over the region near 0106 UTC.

As shown in Fig. 3b, the higher T_B89v observations located between about 55° and 56°N over the Baltic Sea are due to increased WVC and LWC in this region, and the lower T_B89v measurements over water north of about 58.5°N occur in precipitation-free, cloudless regions where the effects of the sea surface's low microwave emissivity are greatest. Pronounced vertically polarized AMSR 89-GHz brightness temperature (T_B89v) depressions were observed in the precipitating regions and were due largely to scattering of upwelling microwave radiation by frozen hydrometeors. These areas of lower T_B89v match up well with increased S_{89} values, which again highlight the importance of volume scattering by precipitation-sized particles (Fig. 3c).

b. Case 2—28 December 2002

The second case chosen for analysis occurred near 1145 UTC 28 December 2002. A large swath of light precipitation associated with a warm-frontal system covered much of the southern half of the Hemse radar domain (Fig. 4a). The maximum radar reflectivity value

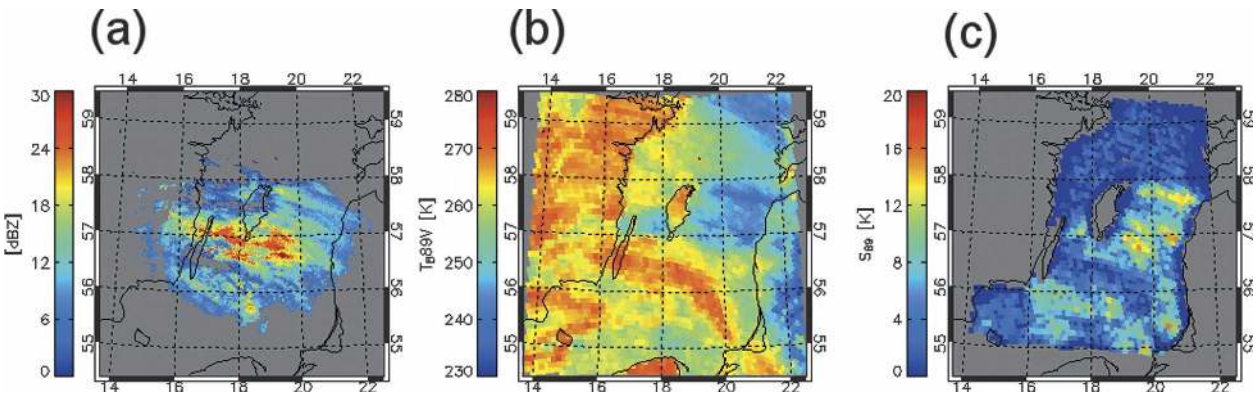

FIG. 4. (a) Hemse radar reflectivity, (b) AMSR-E T_B89V, and (c) AMSR-E S_{89} near 1145 UTC 28 Dec 2002.

was about 32 dBZ, and the approximate average radar echo top was 4.5 km. BALTRAD-derived surface precipitation rates exceeded 3 mm h^{-1} in isolated areas, but most rain rates again were less than 2 mm h^{-1}. Strong north–south gradients in the AMSR-derived freezing level heights (~0.1–1.5 km), WVP (~8–21 kg m^{-2}), and LWP (~0–0.5 kg m^{-2}) indicated the presence of a frontal zone that extended across the region. The NCEP GDAS 2-m temperature near Gotland Island was 2.6°C, with subfreezing temperatures evident far below the 850-hPa level.

Figure 4b reveals depressed AMSR T_B89v readings in the precipitating regions near Gotland Island that correspond to elevated S_{89} values (Fig. 4c). A curved region of higher T_B89v values located south of Gotland Island over the Baltic Sea are due to increased LWC values that exist in a radar reflectivity field gap. Higher LWC amounts to the northwest of Gotland Island in precipitation-free areas also cause relatively higher T_B89v observations. The decreased T_B89v measurements in the far-northeast sector of our observation domain occur in precipitation-free, cloudless regions where the AMSR instrument reading is dominated by the sea surface signature. The *Aqua* satellite overpass of the region was near 1150 UTC, whereas the AMSU-B instrument overpass on *NOAA-17* was near 1208 UTC.

5. Simulation results

a. Comparisons of simulated AMSR-E 89-GHz brightness temperatures

Figure 5 and Fig. 6 compare brightness temperature simulations using the BP2001 parameterization method and the new microphysical parameterizations described in section 3. The top three panels of each figure show scatterplots of AMSR-observed T_B89v fields versus T_B calculated by the BP2001 method for various size ratios x (see BP2001). The bottom panels were created using the new physical parameterization with three different ice crystal models shown in Fig. 3. Note that only data points that are coincident with radar reflectivity values of greater than 0 dBZ are considered in these plots to constrain the comparison to only potentially "precipitating" pixels.

As shown in Fig. 5, the BP2001-based simulations show good correlation with the AMSR T_B89v data for the 12 January 2003 case (between 0.78 and 0.79); minimal biases between −2.6 and −3.6 K are observed, and bias-adjusted RMS errors are between 3.4 and 3.6 K. There is an incremental increase in the magnitude of the biases as the value of x increases from 0.75 to 1.25, similar to the findings presented in BP2001, where scattering by ice particles increases with decreasing prescribed average melted ice-particle radius (when linked to the same exponential DSD of liquid droplets). The optimal value of x, where correlations are highest and the bias-adjusted RMS errors are minimized, appears to be near 1.0. The new physically based method for deriving ice size distributions and optical properties also produces good results when compared with the 12 January 2003 AMSR T_B89v data (bottom panels in Fig. 5). Correlations for the three respective ice habit models are very good; the biases fall between about −3 and −4.5 K, and the bias-adjusted RMS errors are again near 3.4 K. The HC case displays the best results, with the highest correlations and lowest RMS errors. Note the distinct similarity between the modeled HC and $x = 1.0$ results.

Figure 6 displays the modeled and AMSR T_B89v comparisons for the 28 December 2002 case. Correlations are excellent for all simulations (near 0.91), and biases and bias-adjusted RMS errors are also minimal. There are slight differences in the BP2001 simulation

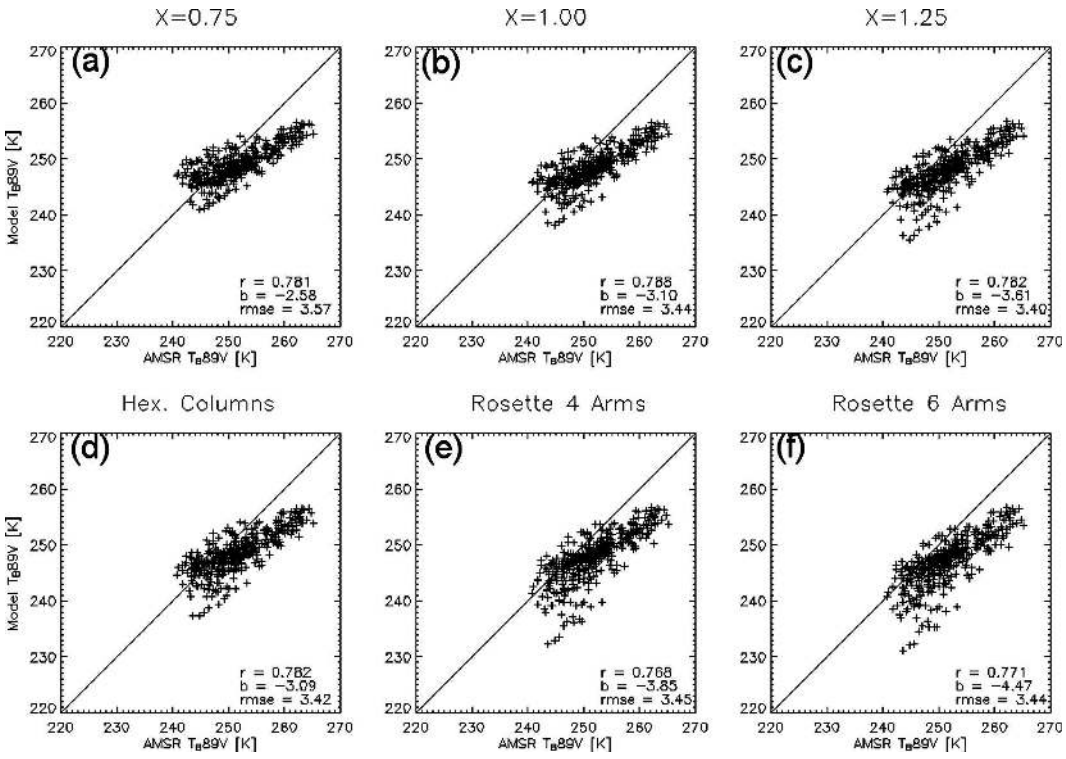

FIG. 5. Scatterplots of modeled vs AMSR-E T_B89V for 12 Jan 2003 based on the BP2001 method for (a) $x = 0.75$, (b) $x = 1.00$, and (c) $x = 1.25$. (d)–(f) Same as (a)–(c), but using the DDA-based microphysics with frozen hydrometeors depicted as (d) hexagonal columns, (e) four-arm rosettes, and (f) six-arm rosettes.

biases when compared with the new microphysical/DDA-based scattering model, though. The BP2001 scheme produces enhanced T_B89v depressions in the most intensely scattering regions (modeled data points near and below 240 K in the scatterplots) that combat the region of higher modeled T_B89v values (modeled data points near 255 K) observed in every simulation, thus reducing the overall bias. Note that the cluster of modeled data points between ~250 and 260 K that are systemically warmer than the AMSR T_B89v observations are mostly located in the far-southwest portion of the radar domain. The behavior of these data points is related to inherent shortcomings in the radar reflectivity used as input and is discussed further in section 6. Also, a set of modeled T_B89v values above 260 K display an obvious cold bias when compared with the AMSR observations. These data points are located in lightly precipitating regions that are strongly affected by background biases (again, see section 6 for further discussion).

b. *Comparisons of simulated AMSU-B 89-GHz brightness temperatures*

Figure 7 and Fig. 8 compare brightness temperature simulations using the BP2001 parameterization method and the new microphysical parameterizations with AMSU-B T_B89 observations. As mentioned in section 2, the footprint sizes of the AMSU-B 89-GHz channel are much larger than those of AMSR. Also, recall that the AMSU-B scanning angle is not constant because it scans in a cross-track fashion. The scanning angle of AMSU-B over the precipitating regions shown in Fig. 7 and Fig. 8 are around 25°–35° and 15°–30°, respectively. Because the AMSU-B overpass time preceded the AMSR overpass by about 25 min, radar data from 0115 UTC were used to construct the precipitation fields for AMSU-B comparisons to minimize temporal sampling errors.

The 89-GHz BP2001-based results for the 12 January 2003 case are correlated well and, like the AMSR comparison, show an obvious sensitivity to increasing x values (top panels in Fig. 7). The "best" size ratio, based on highest correlations and lowest bias-adjusted RMS error, is $x = 0.50$ (Fig. 7a). The optimal size ratio x value differs from the AMSR comparisons, where x between 0.75 and 1.0 was deemed the best fit for this case. The small size ratio implies the mean frozen particle size is large when compared with the mean liquid drop size below the freezing level. This suggests that the BP2001 method cannot generate the consistent bright-

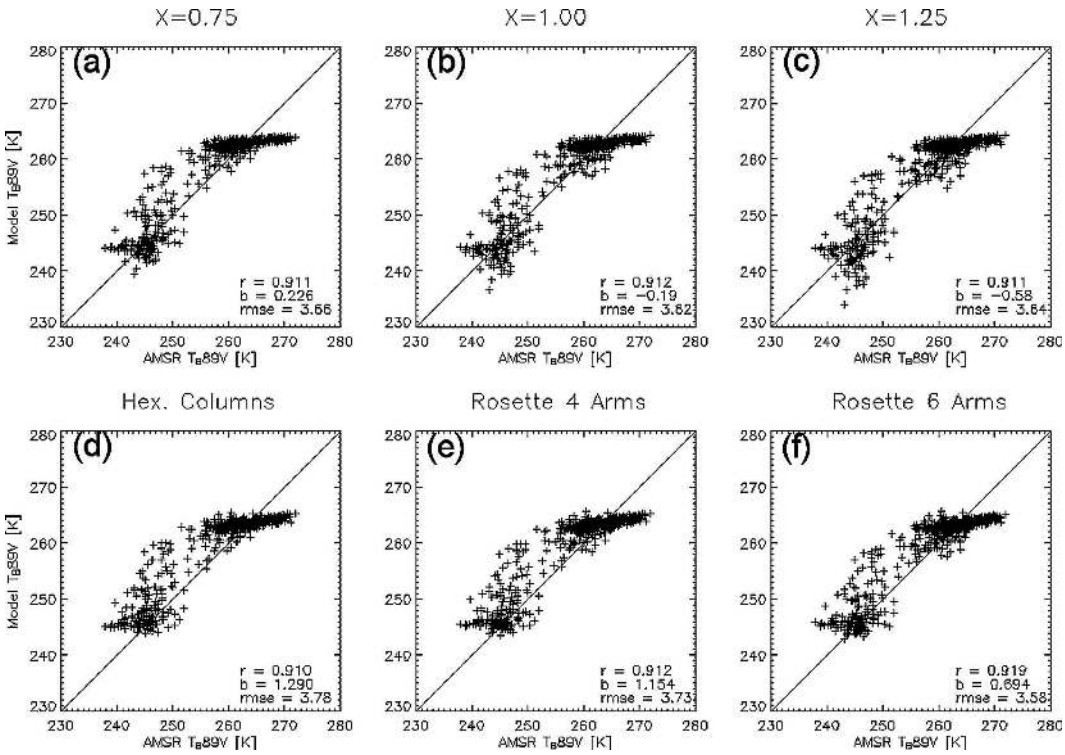

FIG. 6. Same as Fig. 5, but for 28 Dec 2002.

ness temperatures with a unique size ratio x for different instruments with different observation angles and footprint sizes. However, the variations between different size ratios in Figs. 7a–7c are small in comparison with the overall variability seen in the results.

Correlations are generally lower in the DDA-based results at 89 GHz (lower panels in Fig. 7) when compared with the BP2001-based simulations, although higher size ratios using the BP2001 method (not shown) do produce lower correlations that appear very similar to the DDA results displayed in Fig. 7. It is noted that the DDA results do not show significant sensitivity to snow particle shapes, because the correlation, bias, and RMS error values are very similar in all three AMSU-B 89-GHz DDA-based simulations.

All 89-GHz simulations for the 28 December 2002 case compare extremely well to the AMSU-B observations (Fig. 8). The BP2001-based method produces slightly higher correlations and different biases (for the values of x shown) than the new DDA-based results because of the sensitivity of a few modeled data points with T_B89 values between ~230 and 240 K that are located in the regions of highest scattering by frozen particles. Increasing x to large values (not shown) produces similar results to the DDA-based method shown in Fig. 8, similar to the trend observed in the 12 January 2003 case. Last, the modeled DDA results are again fairly insensitive to ice habit type.

c. *Comparisons of simulated AMSU-B 150-GHz brightness temperatures*

Figure 9 and Fig. 10 compare brightness temperature simulations using the BP2001 parameterization method and the new microphysical parameterization with AMSU-B T_B150 observations. For the 12 January 2003 case (Fig. 9), correlations between modeled and AMSU brightness temperatures are lower than the AMSU 89-GHz results using both the BP2001- and DDA-based methods. These lower correlations are due to a cluster of points for which the model results are significantly warmer than the AMSU observations, due at least partially to shortcomings in the radar data input (see section 6 for more details). Correlations and RMS errors between the BP2001 method and the AMSU-B T_B150 values are minimized with an x value of 2.0, which implies that the frozen hydrometeors' melted diameter is very small when compared with the liquid droplets below the freezing level. Recall that x around or lower than 1.00 produced the best comparisons with AMSR T_B89v observations. The DDA-based simulations using HCs and R4s show little sensitivity to habit changes, although the R6 results slightly improve the correla-

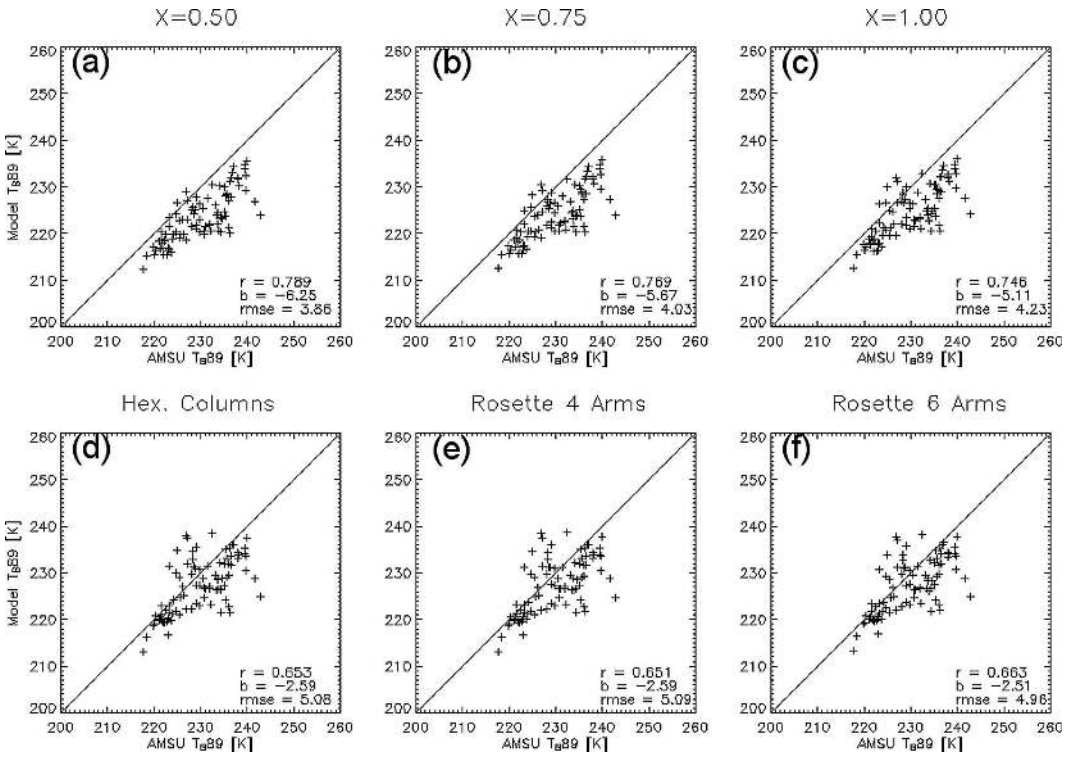

FIG. 7. Same as Fig. 5, except AMSU-B T_B89 data are used in the comparison. The values of x also differ from Fig. 5.

tions and bias-adjusted RMS error values through increased scattering.

Results for the 28 December 2002 case display better correlations and lower RMS errors than the 12 January 2003 case (Fig. 10). For the BP2001 simulations, $x = 2.0$ again produces the best results, and the R6 simulation is the best DDA-based test. Like the previous case, the HC and R4 simulation results are virtually identical. The distinctive pattern displayed in all of the scatterplots in Fig. 10 arises from possible data input issues that are discussed in section 6.

6. Discussion

The results highlighted in the previous section illustrate that the BP2001 and new parameterization methods can both generate brightness temperatures consistent with AMSR and, to a lesser extent, AMSU-B observations. In fact, the 12 January 2003 modeled versus observed AMSR T_B89v comparisons for $x = 1.0$ (Fig. 5b) and HC (Fig. 5d) are virtually identical, even though different representations of ice PSDs, shapes, and scattering properties were employed. Therefore, one might conclude that using Mie theory with equivalent spherical particles to represent the frozen hydrometeors (as done in BP2001) might be suitable for performing radiative transfer modeling for these winter-precipitation cases. However, note that the optimal size ratio values using the BP2001 method are below 1.0 for 89 GHz but are around 2.0 for AMSU-B T_B150 comparisons. One unique size ratio value cannot produce consistent brightness temperatures for different frequencies and/or sensor resolutions. This result suggests that the BP2001 method cannot generate physically consistent brightness temperatures based on the same radar reflectivity fields used as input, because the derived ice water content differs for varying frequencies. To illustrate this point, Fig. 11 shows the radar reflectivity versus derived frozen water content for the 12 January 2003 case using the optimal x values for the AMSR and AMSU-B comparisons, plus the HC simulation. Therefore, we can conclude that the use of fluffy spheres, even including an empirical scaling (as done in BP2001), has potential limitations when retrieving ice water content and/or precipitation rate using brightness temperatures provided by different channels of passive microwave radiometers.

As mentioned in section 5, other issues unrelated to the microphysical and scattering representation of frozen hydrometeors affect the radiative transfer simula-

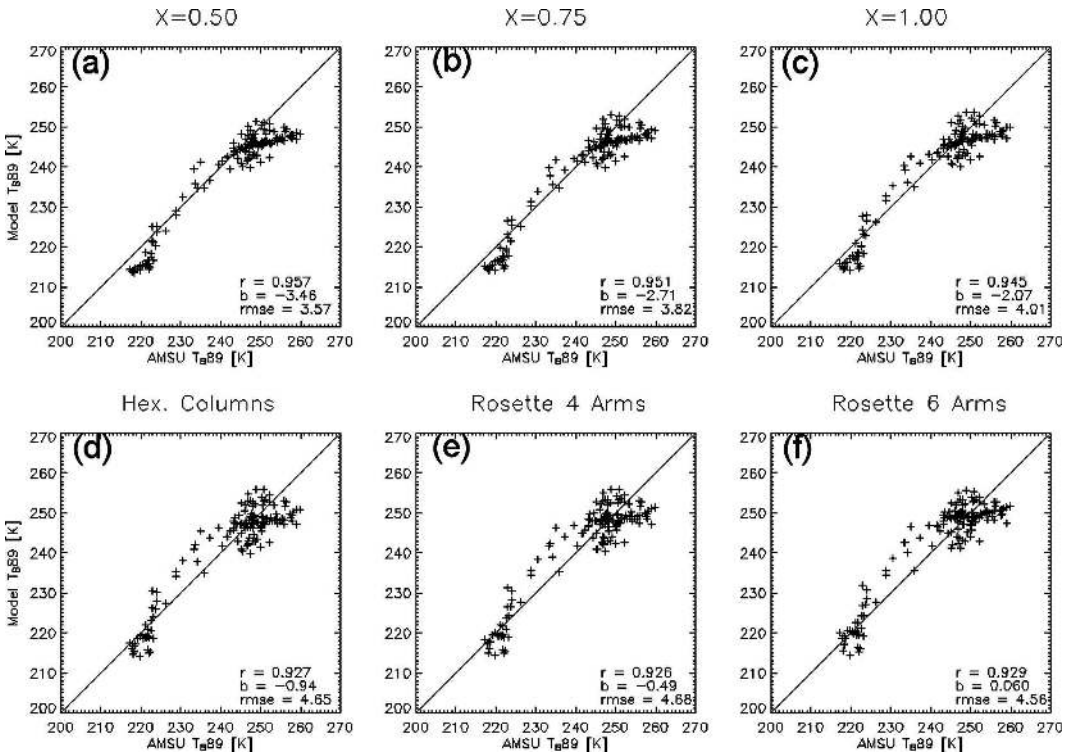

FIG. 8. Same as Fig. 6, except AMSU-B T_B89 data are used in the comparison. The values of x also differ from Fig. 6.

tions. First, there are inherent errors in the background fields that strongly influence the modeled results. Figure 12 depicts the brightness temperature comparisons between various simulations and AMSR/AMSU-B observations for pixels not associated with precipitation. Obvious environmental biases are apparent in Fig. 12 for both of the case studies. These biases are reflected in Figs. 5–10, especially for data points in the scatterplots that are associated with very light precipitation. The 12 January 2003 case shows consistent negative biases in nonprecipitating regions for all of the sensors and frequencies considered (Fig. 12, top panels). The major sources of these background biases are related to surface emissivity errors due to the extremely low salinity of the Baltic Sea, as well as possible surface temperature and wind speed errors. Potential errors in our derived LWC, WVC, and vertical temperature fields also exist. The brightness temperature differences caused by the surface emissivity error alone can account for potentially up to a few kelvins in nonprecipitating regions. However, they only marginally affect the results in the precipitating regions because the optically thick atmosphere screens out the surface effect at frequencies greater than 90 GHz (see Fig. 3.17 in section 3.4.5 of Janssen 1993).

The 28 December 2002 example displays a bimodal structure in the nonprecipitating brightness temperature comparisons (Fig. 12, bottom panels). Negative biases similar to the 12 January 2003 case exist in the lower to midranges of the background brightness temperatures. However, a region of skewed warmer brightness temperatures behaves much differently. This artifact is likely due to an improperly represented LWC field in the southeast region of our model domain where a LWC maximum exists. This feature also shows up prominently in the precipitating pixels plotted in Figs. 6, 8, and 10.

In addition to the errors associated with the background fields used in the radiative transfer modeling, the radar reflectivity data used to construct precipitation profiles also have limitations that must be considered. Radar data are inherently sensitive to calibration issues. Even though no known calibration problems exist with the radar dataset used in this study, even minor calibration errors could significantly affect our results, and its mere possibility should be mentioned.

In addition to calibration issues, range effects also influence the model results. For instance, the 28 December 2002 simulations display a collection of points that are consistently warmer than the AMSR T_B89v (Fig. 6) and AMSU-B T_B150 (Fig. 10) measurements. Many of these data points are located in lightly precipi-

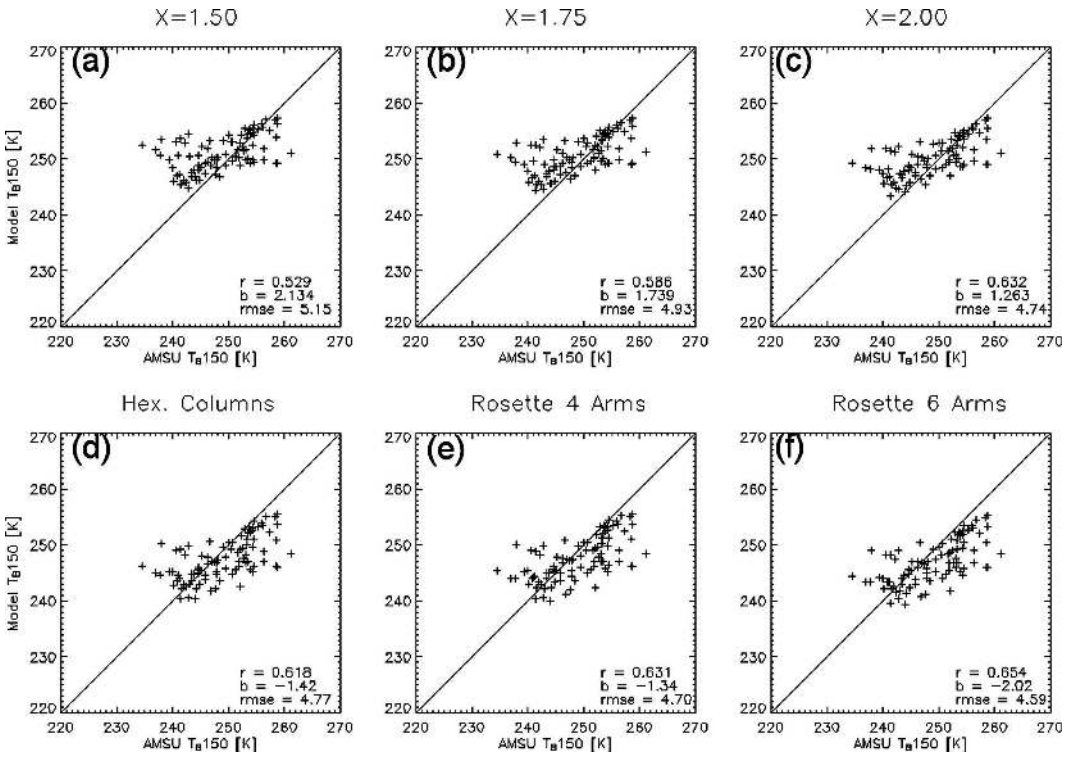

FIG. 9. Same as Fig. 5, but for AMSU-B T_B150. Note also that the three x values in (a)–(c) differ from Figs. 5a–c.

tating regions in the far-southwest section of the radar domain where the radar beam is undoubtedly overshooting some of the light precipitation. Therefore, the reflectivity profiles (and thus the derived frozen precipitation contents) are most likely underestimated in these regions and suppress the scattering effects of frozen hydrometeors. These warm modeled data points should therefore not be construed as a limitation of the microphysical and/or scattering models employed but rather as a potential data input problem that needs to be improved. Note that these radar range effects are somewhat mitigated by elevating the size ratio using the BP2001 method (e.g., Fig. 10c). Increasing the size ratio to large levels, however, artificially inflates the columnar ice content and produces more desirable, yet probably unphysical, results.

A last radar-related complication is evident in the 12 January 2003 model comparisons with AMSU T_B150 observations shown in Fig. 9. A group of warmer modeled data points greatly skews the statistics for this case. Detailed analysis of these points indicates that most correspond to depressed radar reflectivity measurements above 2 km that are artifacts produced by the pseudo-CAPPI procedure used in this study (not shown, but see Fig. 7 in BP2001 for an example of these artifacts). These points are located within a reasonable distance from the radar, and so range effects should not adversely affect the reflectivity values. A first-order correction was applied to the data levels that displayed the ringed reflectivity artifacts by assuming a reflectivity profile similar to that discussed by Pohjola and Koistinen (2002), who compiled climatological statistics of vertical reflectivity structure for winter precipitation events in Finland. Marked improvements in the T_B150 scatterplots were observed in some of the warmest modeled data points (not shown). The T_B89 results were not as sensitive to the corrected reflectivity values as were T_B150 results, although improvements (not shown) were made relative to the plots shown in Fig. 7. These results are not surprising, because even small changes in ice water content should produce larger changes in the 150-GHz frequency results because this frequency has been demonstrated to be much more sensitive to scattering by ice than is 89 GHz (Bennartz and Bauer 2003).

On a final cautionary note, the AMSU-B results must be interpreted carefully because of some important factors. First, because the AMSU-B instrument uses a cross-track-scanning technique, the local zenith angle can change dramatically over the scene of interest. This fact is immediately evident when comparing the AMSR (Fig. 5a) and AMSU-B (Fig. 7a) 89-GHz scatterplots

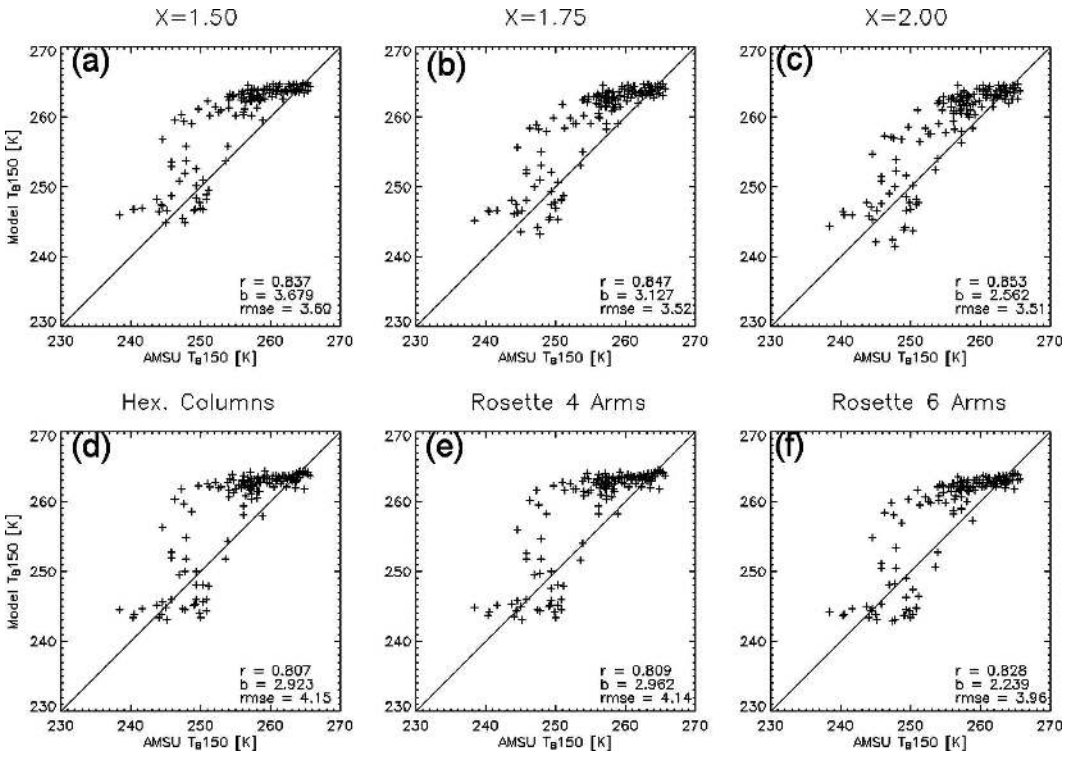

FIG. 10. Same as Fig. 6, except AMSU-B T_B150 data are used in the comparison. The values of x also differ from Fig. 6.

for the 12 January 2003 case. The minimum T_B89 values for each instrument are near 240 and 215 K, respectively. The lowest AMSR T_B89v measurements are located in the regions where scattering effects dominate. The lowest AMSU-B T_B89 readings, though, occur on the northern fringes of the precipitation shield outside of the most intensive scattering areas. The zenith angle is near 35° in these regions, thus creating a much more direct path through the atmosphere to the sea surface that allows the effects of the low sea surface emissivity to strongly affect the measurement. The AMSU-B footprint is also much larger than that of the AMSR and varies in size, and the convolved model results are averaged over much larger spatial region. Therefore, the environmental biases may strongly influence the simulation results, especially in areas of light precipitation near the edges of the precipitation shield where nonprecipitating pixels are more frequently utilized in the AMSU-B convolution process.

7. Summary and conclusions

This study presents a new physically based approach to model scattering by ice particles at microwave frequencies. The main features of the new scheme are that 1) temperature-dependent ice PSDs measured by aircraft in midlatitude frontal systems (Field et al. 2005) are used to represent the distribution of precipitation-sized frozen hydrometeors above the freezing level through derived radar reflectivity–snow-water content relationships and 2) the discrete dipole approximation is employed to calculate optical properties of selected types of idealized nonspherical ice particles (hexagonal columns, four-arm rosettes, and six-arm rosettes).

Passive microwave optical properties were derived from precipitation profiles of two light-winter-precipitation cases. The precipitation profiles were generated from ground-based radar observations from Gotland Island in the Baltic Sea. Forward radiative transfer simulations of these cases were compared with AMSR and AMSU-B microwave measurements to assess the new model's performance. Also, radiative transfer model output comparisons were made with the method outlined in BP2001 that models frozen hydrometeors as equivalent spheres, uses Mie theory to calculate optical properties, and prescribes a Marshall–Palmer-type DSD for frozen particles that is linked to the liquid hydrometeor distribution below the melting level by a size ratio x. There are four major findings of these simulations:

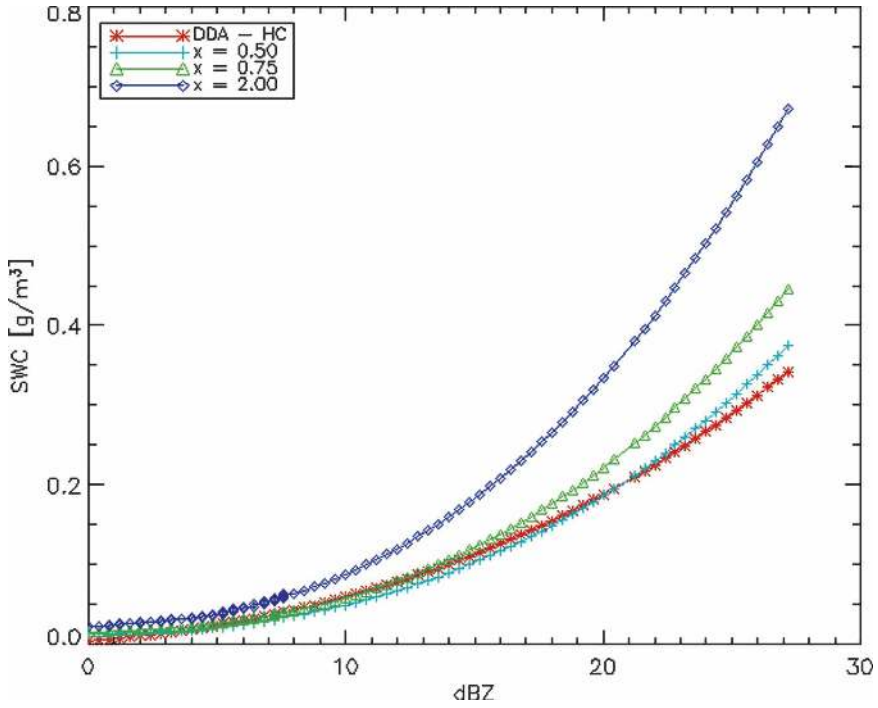

FIG. 11. BALTRAD observed radar reflectivity (dBZ) and derived ice water content M with BP2001 method and the new parameterization method of this study. Crosses, triangles, and diamonds represent the results from the BP2001 method with $x = 0.5$, $x = 1.0$, and $x = 2.0$, respectively. The red asterisks represent the DDA results using hexagonal columns.

1) The new ice scattering/microphysics model was able to generate brightness temperatures that were consistent with AMSR and AMSU-B observations of two light-winter-precipitation cases, especially when considering the errors and complications associated with calculating various environmental parameters (sea surface emissivity, LWC, etc.) and the limitations of radar data (e.g., range effects or artifacts introduced by radar scan geometry and the pseudo-CAPPI approach).
2) Hexagonal columns produced the best match with AMSR T_B89v observations for one case study, and six-arm rosettes created optimal comparisons with AMSR T_B89v data for the second case study. The overall differences between the various ice habit results at 89 GHz are generally not that expansive, however, which leaves open the possibility of using one habit type to model all frozen hydrometeors at this frequency without introducing large errors.
3) The new model results are relatively insensitive to ice habit type when compared with the AMSU-B 89-GHz data. The AMSU-B 150-GHz comparisons are also mostly insensitive to either the hexagonal column or four-arm rosette ice habit type. Higher sensitivity is observed when the more-complex-shaped six-arm rosette ice habit is applied, though, and the results are slightly better at 150 GHz using six-arm rosettes.
4) In each case study, the use of fluffy spheres (as done in BP2001) produces differing radiances and derived snow water content depending on what frequency and/or sensor resolution is used. Although the BP2001 method is able to produce similar overall brightness temperature comparisons with microwave sensor data through its ability to tune the ice PSD, it may generate results that are inconsistent, especially if multifrequency passive microwave observations are used.

Although there is an obvious need to analyze more cases to test further the new model's robustness, the initial results are encouraging because they demonstrate the model's potential application to light-winter-precipitation events that have not been extensively studied using microwave remote sensing techniques. The ice habit types used for our DDA calculations are admittedly very idealized, and therefore future work will incorporate more-complex frozen particle shapes. We also constrain our model to use one type of ice habit for all frozen particles, which is a simplification of the potential myriad of ice-habit combinations that may be found in the atmosphere. Strategies will be explored

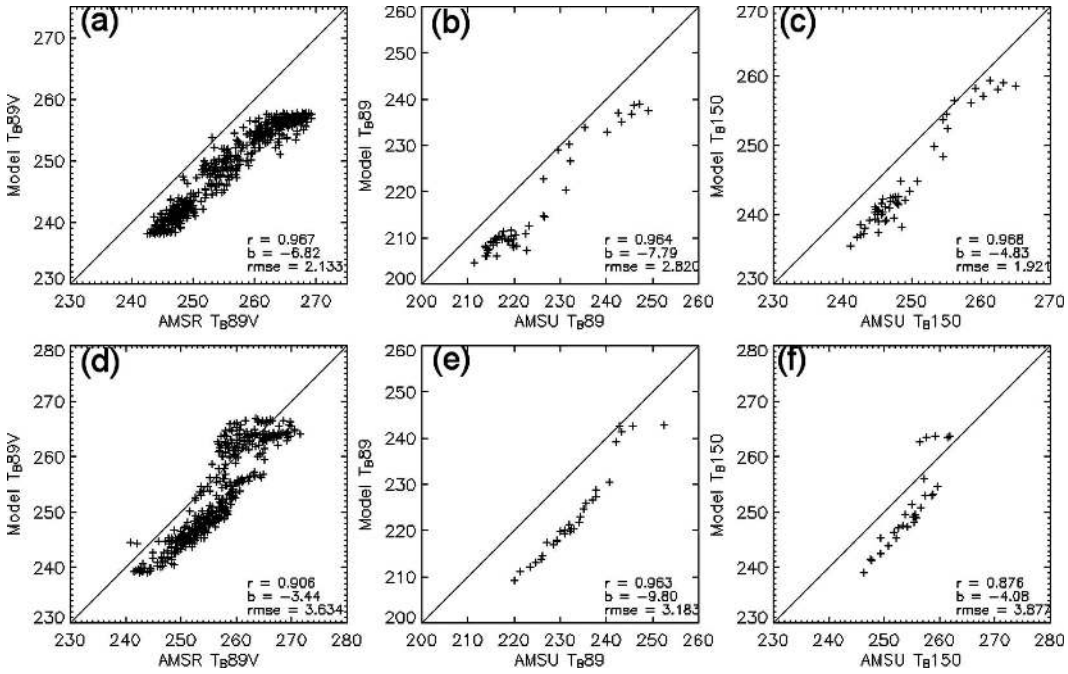

FIG. 12. Comparison of (a) AMSR-E T_B89V, (b) AMSU-B T_B89, and (c) AMSU-B T_B150 vs simulated 12 Jan 2003 results for "nonprecipitating" pixels. (d)–(f) Same as (a)–(c), but for the 28 Dec 2002 case.

that will address, it is hoped, the distribution of shapes within frozen precipitation profiles. Despite these shortcomings, this study provides a physically based framework that should be useful for future microwave remote sensing applications of frozen precipitation.

Acknowledgments. The authors are indebted to Daniel B. Michelson at the Swedish Meteorological and Hydrological Institute for providing the BALTRAD radar data and to Grant W. Petty for many useful discussions. We also thank three anonymous reviewers for their constructive comments. This work was funded by NASA Grant NAG5-12579. Support from the Wisconsin Space Grant Consortium is also gratefully acknowledged.

REFERENCES

Bauer, P., J. P. V. Poiares Baptista, and M. de Iulis, 1999: The effect of the melting layer on the microwave emission of clouds over the ocean. *J. Atmos. Sci.,* **56,** 852–867.

Bennartz, R., 2000: Optimal convolution of AMSU-B to AMSU-A. *J. Atmos. Oceanic Technol.,* **17,** 1215–1225.

——, and G. W. Petty, 2001: The sensitivity of microwave remote sensing observations of precipitation to ice particle size distributions. *J. Appl. Meteor.,* **40,** 345–364.

——, and P. Bauer, 2003: Sensitivity of microwave radiances at 85–183 GHz to precipitating ice particles. *Radio Sci.,* **38,** 8075, doi:10.1029/2002RS002626.

——, A. Thoss, A. Dybbroe, and D. B. Michelson, 2002: Precipitation analysis using the advanced microwave sounding unit in support of nowcasting applications. *Meteor. Appl.,* **9,** 177–189.

Chen, F. W., and D. H. Staelin, 2003: AIRS/AMSU/HSB precipitation estimates. *IEEE Trans. Geosci. Remote Sens.,* **41,** 410–417.

Deblonde, G., and S. English, 2000: Evaluation of the FASTEM2 fast microwave oceanic surface emissivity model. *Proc. 11th Int. ATOVS Study Conf.,* Budapest, Hungary, Bureau of Meteorology Research Centre, 67–78.

Draine, B. T., 1988: The discrete dipole approximation and its application to interstellar graphite grains. *Astrophys. J.,* **333,** 848–872.

——, and P. J. Flatau, 1994: Discrete dipole approximation for scattering calculations. *J. Opt. Soc. Amer. A,* **11,** 1491–1499.

——, and ——, cited 2003: User guide for the discrete dipole approximation code DDSCAT 6.0. 59 pp. [Available online at http://arxiv.org/abs/astro-ph/0409262v2.]

English, S. J., and T. J. Hewison, 1998: A fast generic millimeter-wave emissivity model. *Microwave Remote Sensing of the Atmosphere and Environment,* T. Hayasaka et al., Eds., International Society for Optical Engineering (SPIE Proceedings Vol. 3503), 288–300.

Field, P. R., R. J. Hogan, P. R. A. Brown, A. J. Illingworth, T. W. Choularton, and R. J. Cotton, 2005: Parameterization of ice particle size distributions for mid-latitude stratiform cloud. *Quart. J. Roy. Meteor. Soc.,* **131,** 1997–2018.

Fujiyoshi, Y., T. Endoh, T. Yamada, L. Tsuboki, Y. Tachibana, and G. Wakahama, 1990: Determination of a *Z–R* relationship for snowfall using a radar and high sensitivity snow gauges. *J. Appl. Meteor.,* **29,** 147–152.

Heymsfield, A. J., and C. M. R. Platt, 1984: A parameterization of the particle size spectrum of ice clouds in terms of the ambi-

ent temperature and the ice water content. *J. Atmos. Sci.,* **41,** 846–855.

——, A. Bansemer, P. R. Field, S. L. Durden, J. L. Stith, J. E. Dye, W. Hall, and C. A. Grainger, 2002: Observations and parameterizations of particle size distributions in deep tropical cirrus and stratiform precipitating clouds: Results from in situ observations in TRMM field campaigns. *J. Atmos. Sci.,* **59,** 3457–3491.

Hobbs, P. V., S. Chang, and J. D. Locatelli, 1974: The dimensions and aggregation of ice crystals in natural clouds. *J. Geophys. Res.,* **79,** 2199–2206.

Illingworth, A. J., and T. M. Blackman, 1999: The need to normalize PSDs based on the gamma PSD formulations and implications for interpreting polarimetric radar data. Preprints, *29th Int. Conf. on Radar Meteorology,* Montreal, QC, Canada, Amer. Meteor. Soc., 629–631.

Janssen, M. A., 1993: *Atmospheric Remote Sensing by Microwave Radiometry.* John Wiley and Sons, 572 pp.

Johnson, B. T., and G. W. Petty, 2004: Improving mid to high latitude passive microwave retrievals and simulations of precipitation using aircraft based Doppler radar data. Preprints, *13th Conf. on Satellite Meteorology and Oceanography,* Norfolk, VA, Amer. Meteor. Soc., P8.21.

Katsumata, M., H. Uyeda, K. Iwanami, and G. Liu, 2000: The response of 36- and 89-GHz microwave channels to convective snow clouds over ocean: Observation and modeling. *J. Appl. Meteor.,* **39,** 2322–2334.

Kim, M.-J., 2006: Single scattering parameters of randomly oriented snow particles at microwave frequencies. *J. Geophys. Res.,* **111,** D14201, doi:10.1029/2005JD006892.

Kongoli, C., P. Pellegrino, R. Ferraro, N. Grody, and H. Meng, 2003: A new snowfall detection algorithm over land using measurements from the Advanced Microwave Sounding Unit (AMSU). *Geophys. Res. Lett.,* **30,** 1756, doi:10.1029/2003GL017177.

Lee, G., I. Zawadzki, W. Szyrmer, D. Sempere-Torres, and R. Uijlenhoet, 2004: A general approach to double-moment normalization of drop size distributions. *J. Appl. Meteor.,* **43,** 264–281.

Liu, G., 2004: Approximation of single scattering properties of ice and snow particles for high microwave frequencies. *J. Atmos. Sci.,* **61,** 2441–2456.

——, and J. A. Curry, 1997: Precipitation characteristics in the GIN seas determined using satellite microwave data. *J. Geophys. Res.,* **102,** 13 987–13 997.

Marshall, J. S., and W. M. K. Palmer, 1948: The distribution of raindrops with size. *J. Meteor.,* **5,** 165–166.

Mätzler, C., and U. Wegmüller, 1987: Dielectric properties of fresh-water ice at microwave frequencies. *J. Phys. D,* **20,** 1623–1630.

Michelson, D. B., and Coauthors, 2000: BALTEX radar data centre products and their methodologies. SMHI Reports of Meteorology and Climatology (RMK) No. 90, SMHI, 76 pp.

——, J. Koistinen, R. Bennartz, C. Fortelius, and A. Thoss, 2002: BALTEX radar achievements at the end of the main experiment. *Proc. Second European Conf. on Radar Meteorology,* Delft, Netherlands, Copernicus GmbH, 357–362.

Mishchenko, M. I., J. W. Hovenier, and L. D. Travis, 2000: *Light Scattering by Nonspherical Particles*. Academic Press, 690 pp.

Petty, G. W., 1994a: Physical retrievals of over-ocean rain rate from multichannel microwave imagery. Part 1: Theoretical characteristics of normalized polarization and scattering indices. *Meteor. Atmos. Phys.,* **54,** 79–100.

——, 1994b: Physical retrievals of over-ocean rain rate from multichannel microwave imagery. Part 2: Algorithm implementation. *Meteor. Atmos. Phys.,* **54,** 101–121.

Pohjola, H., and J. Koistinen, 2002: Diagnostics of vertical reflectivity profiles at the radar sites. *Proc. Second European Conf. on Radar Meteorology,* Delft, Netherlands, Copernicus GmbH, 233–237.

Saunders, R. W., T. J. Hewison, N. C. Atkinson, and S. J. Stringer, 1995: The radiometric characterization of AMSU-B. *IEEE Trans. Microwave Theory Technol.,* **43,** 760–771.

Sekhon, R. S., and R. C. Srivastava, 1970: Snow size spectra and radar reflectivity. *J. Atmos. Sci.,* **27,** 299–307.

Tinel, C., J. Testud, J. Pelon, R. J. Hogan, A. Protat, J. Delanoe, and D. Bouniol, 2005: The retrieval of ice-cloud properties from cloud radar and lidar synergy. *J. Appl. Meteor.,* **44,** 860–875.

Wentz, F. J., 1997: A well-calibrated ocean algorithm for special sensor microwave/imager. *J. Geophys. Res.,* **102,** 8703–8718.

Westbrook, C. D., R. C. Ball, P. R. Field, and A. J. Heymsfield, 2004a: Universality in snowflake aggregation. *Geophys. Res. Lett.,* **31,** L15104, doi:10.1029/2004GL020363.

——, ——, ——, and ——, 2004b: A theory of growth by differential sedimentation, with application to snowflake formation. *Phys. Rev. E.,* **70,** 021 403, doi:10.1103/PhysRevE.70.021403.